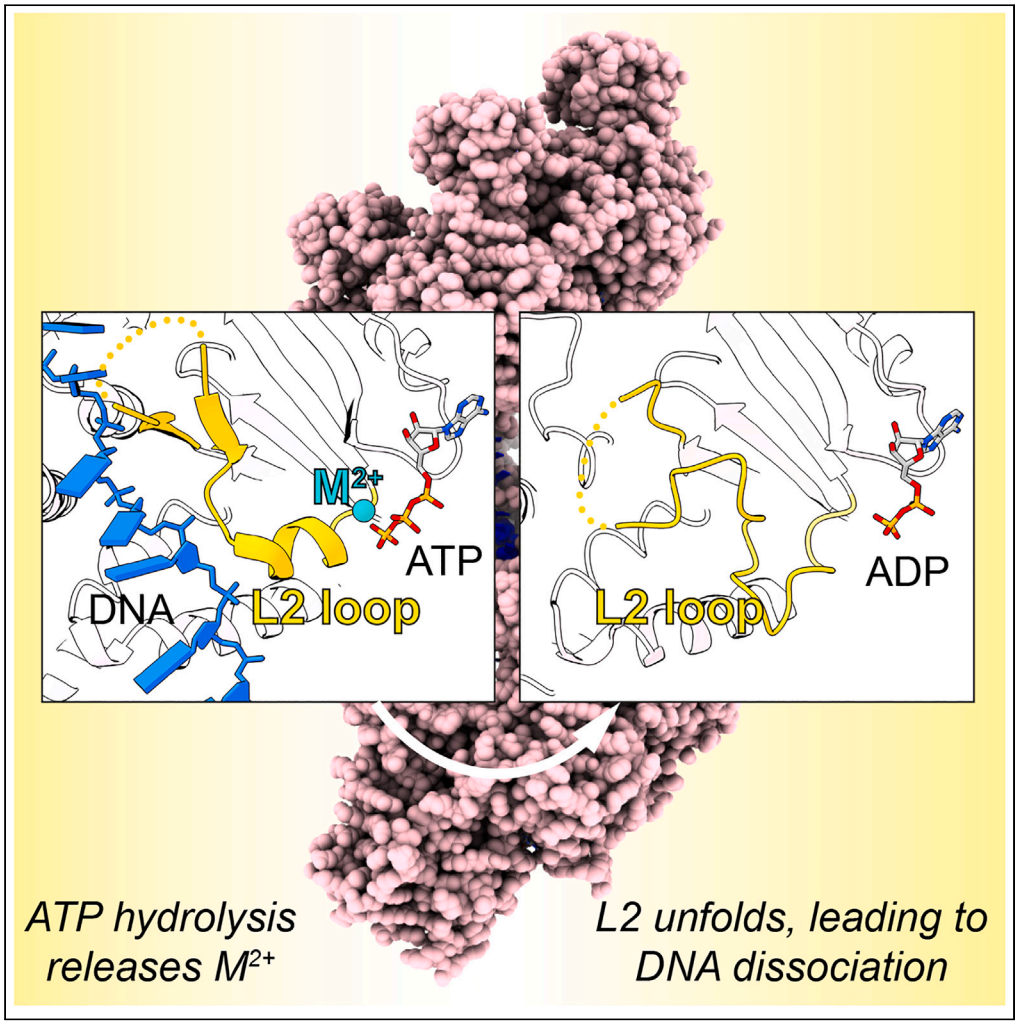
iScience

CellPress
OPEN ACCESS

Article

A metal ion-dependent mechanism of RAD51 nucleoprotein filament disassembly



Robert Appleby, Daniel Bollschweiler, Dimitri Y. Chirgadze, Luay Joudeh, Luca Pellegrini

lp212@cam.ac.uk

Highlights

A second metal ion is bound to ATP in the human RAD51 nucleoprotein filament

The metal ion stabilizes the conformation of RAD51's DNA-binding loop L2

ATP hydrolysis causes metal ion release and L2 unfolding, promoting DNA dissociation

Appleby et al., iScience 26, 106689
May 19, 2023 © 2023 The Authors.
https://doi.org/10.1016/j.isci.2023.106689

iScience

CellPress
OPEN ACCESS

Article

A metal ion-dependent mechanism of RAD51 nucleoprotein filament disassembly

Robert Appleby,[1] Daniel Bollschweiler,[1,2] Dimitri Y. Chirgadze,[1] Luay Joudeh,[1] and Luca Pellegrini[1,3,*]

SUMMARY

The RAD51 ATPase polymerizes on single-stranded DNA to form nucleoprotein filaments (NPFs) that are critical intermediates in the reaction of homologous recombination. ATP binding maintains the NPF in a competent conformation for strand pairing and exchange. Once strand exchange is completed, ATP hydrolysis licenses the filament for disassembly. Here we show that the ATP-binding site of the RAD51 NPF contains a second metal ion. In the presence of ATP, the metal ion promotes the local folding of RAD51 into the conformation required for DNA binding. The metal ion is absent in the ADP-bound RAD51 filament, that rearranges in a conformation incompatible with DNA binding. The presence of the second metal ion explains how RAD51 couples the nucleotide state of the filament to DNA binding. We propose that loss of the second metal ion upon ATP hydrolysis drives RAD51 dissociation from the DNA and weakens filament stability, contributing to NPF disassembly.

INTRODUCTION

Maintenance of genomic stability in bacteria, archaea, and eukaryotes depends critically on the ability to exchange strands between homologous DNA molecules in a reaction known as homologous recombination (HR). The steps of HR comprise the invasion of a target duplex DNA by a single-stranded (ss) DNA segment, followed by search for sequence homology, strand pairing between complementary DNA sequences, and strand exchange.[1,2] Different flavors of HR intervene during various processes of nucleic acid metabolism, such as double-strand break repair,[3,4] DNA replication,[5,6] and the crossover reaction of meiotic prophase.[7,8]

A highly conserved superfamily of ATPases—including eukaryotic RAD51, archeal RadA, and bacterial RecA as representative members—catalyzes the strand-exchange reactions of HR. These strand-exchange proteins (recombinases) polymerize on the single-stranded DNA generated from the controlled resection of DNA ends, forming a helical nucleoprotein filament (NPF). The NPF executes the strand invasion of the target double-stranded (ds) DNA, to form a three-strand intermediate (synapsis), within which the search for homology and strand exchange takes place. Given its central role in DNA metabolism and genomic stability, the biochemical reaction of HR has been the focus of intense research efforts over the past 30 years.

Earlier X-ray crystallography and electron microscopy studies of HR recombinases elucidated the helical features of their filamentous structures, demonstrating that bound DNA was both stretched and underwound.[9–13] The crystallographic studies culminated in the determination of the NPF structure of bacterial RecA, which illustrated how the phosphodiester backbone of the ssDNA is embedded within the protein sheath of the polymeric recombinase, while the bases project outwards toward the solvent, poised for the homology search.[14] The recent development of modern cryoEM approaches has made it easier to image at high resolution the interaction of eukaryotic RAD51 with the DNA within the NPF.[15] These studies showed that the RecA and RAD51 filaments adopt a common mechanism of DNA interaction; the L1 and L2 loops protruding from adjacent ATPase domains grip the DNA strand, unstacking the bases at each protomer interface, and partitioning the nucleotides into triplets.

ATP binding and hydrolysis are essential for RAD51 function. ATP binds at the protomer-protomer interface in the RAD51 filament and promotes the adoption of a filament conformation that is competent for the strand pairing and exchange reactions.[15] ATP hydrolysis is not required for activity *in vitro* as RAD51's Walker A mutants defective in ATP hydrolysis can mediate strand exchange[16,17]; moreover,

[1]Department of Biochemistry, University of Cambridge, Cambridge CB2 1GA, UK

[2]Present address: Max Planck Institute of Biochemistry, CryoEM facility, Am Klopferspitz 18, 82152 Planegg, Germany

[3]Lead contact

*Correspondence: lp212@cam.ac.uk

https://doi.org/10.1016/j.isci.2023.106689

This is an open access article under the CC BY license (http://creativecommons.org/licenses/by/4.0/).

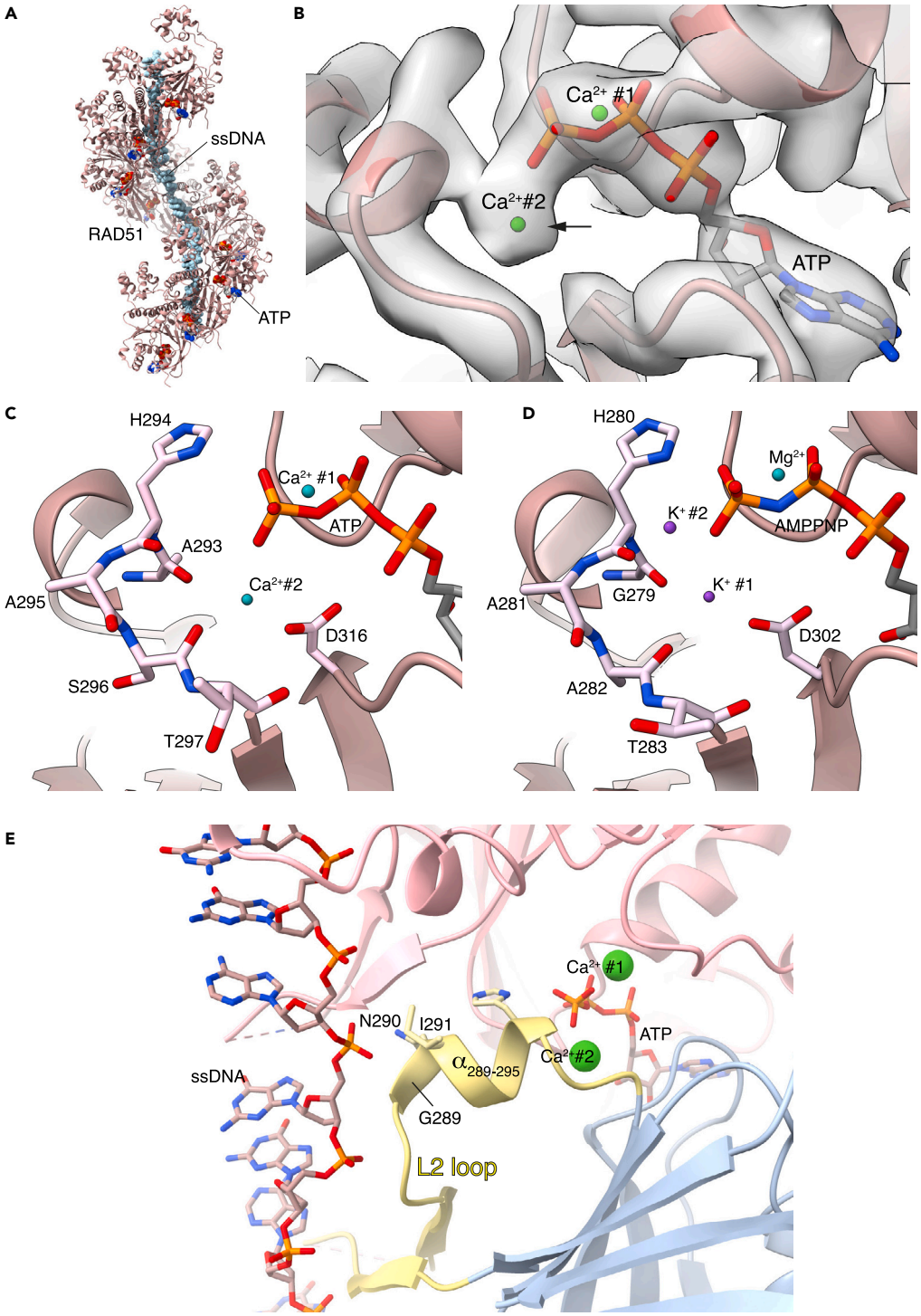


Figure 1. The second metal cation in the pre-synaptic RAD51 filament

(A) CryoEM structure of the human RAD51-ssDNA-ATP filament. RAD51 is shown as ribbons, ssDNA and ATP as spacefill models.

(B) CryoEM map at the ATP site, with the density peak for the second Ca^{2+} ion marked by an arrow. The two Ca^{2+} cations are drawn as green spheres.

(C) Molecular details of the interactions of the second Ca^{2+} cation with ATP and with main-chain and side-chain atoms of surrounding RAD51 residues. The two Ca^{2+} cations are drawn as green spheres. The amino acids that interact with Ca^{2+} and ATP are shown in stick representation. The rest of the RAD51 is drawn as a light brown ribbon.

(D) Molecular details of the interactions of the two K^{+} cations with AMP-PNP and surrounding main-chain and side-chain residues of the archeal RAD51-ortholog RadA (PDB ID 2FPM). The protein and ATP are drawn as in panel C, the two K^{+} cations are shown as purple spheres, the Mg^{2+} cation in green.

Figure 1. *Continued*

(E) The RAD51 α-helix spanning residues 289 to 295 of the L2 loop couples DNA binding to ATP. The second Ca^{2+} cation stabilizes the helical conformation of L2 $\alpha_{289\text{-}295}$ by interacting with the C-terminal end of the helix. The two RAD51 protomers are shown as ribbons in pink and light blue. The conformation of the L2 loop is highlighted in pale yellow, with the two Ca^{2+} cations drawn as green spheres. The ssDNA is drawn in stick representation and colored according to atom type. The side chains of amino acids N290 and I291 at the N-end of the L2 $\alpha_{289\text{-}295}$ and of H294 at the C-end are drawn explicitly.

inhibition of ATP hydrolysis using Ca^{2+} or a non-hydrolyzable ATP analog potentiates strand-exchange activity by keeping the filament in a competent state for recombination.[18] However, the ability to hydrolyze ATP is clearly critical *in vivo*,[19–21] pointing to its importance in the completion of HR in cells. Biochemical evidence shows that that ATP hydrolysis causes RAD51 release from DNA and is necessary for filament disassembly[22–25]: the requirement for ATP hydrolysis is therefore explained by the need to remove RAD51 from DNA once recombination is completed. Dissociation of RAD51 protomers is thought to proceed from the ends of the filament by RAD51 molecules that have hydrolyzed their ATP to ADP.[25] As ATP hydrolysis happens randomly throughout the filament, disassembly takes place by bursts of ADP-bound RAD51 molecules at the filament end, until the next ATP-bound RAD51 becomes terminal.[25]

The consequence of ATP hydrolysis on the RAD51 NPF structure and why it should license its disassembly is unclear. Crystallographic analysis of the archeal RAD51-ortholog RadA bound to the non-hydrolyzable ATP-homolog AMP-PNP had shown the presence of a potassium ion at the ATP-binding site, in contact with the gamma phosphate and making bridging interactions with the neighboring RadA protomer in the crystallographic filament.[26,27] The position and range of interactions of the potassium ion suggested a role for it in organizing the L2 loop of the neighboring RadA molecule in a conformation competent for DNA binding, in agreement with the known stimulatory effects of monovalent cations on DNA binding and strand-exchange activity.[28,29]

Here we used high-resolution cryoEM to investigate the possible presence and functional role of a second metal ion in pre- and post-synaptic RAD51 NPFs. We find that the ATP-binding site contains a second metal ion, in addition to the canonical ion bound within the Walker A motif, in analogous position to the potassium ion observed in the crystal structure of RadA. We further show that loss of the second metal ion in the cryoEM structure of the ADP-bound RAD51 filament leads to a conformational rearrangement in the L2 loop that renders it incompatible with DNA binding. Thus, ATP hydrolysis drives a conformational transition of the filament to a state that is unable to bind DNA and weakens RAD51 self-association, licensing the NPF for disassembly.

RESULTS

A second metal ion at the ATP site of the pre-synaptic RAD51 filament

We determined the cryoEM structure of human RAD51 bound to a ssDNA 60mer and Ca^{2+}ATP at 3.8 Å resolution (Figures 1A and S1, Table S1, STAR Methods). Inspection of the density map at the ATP-binding site showed the presence of a peak near the gamma phosphate and at the interface with the neighboring RAD51 protomer, which was not accounted for by the known features of the ATP ligand and its protein-binding moieties (Figure 1B). In addition to the gamma phosphate, the density peak was surrounded by the main-chain carbonyl groups of A293, H294, and S296 and by the side-chain carboxylate of D316 in the ATPase domain of the adjacent RAD51 protomer (Figure 1C). The position of the peak was analogous to that of the potassium ion bound in the crystal structure of archeal RadA[27] (Figure 1D). The presence of negatively charged oxygen moieties in suitable positions to act as ligands for a divalent metal ion supported the presence of a previously unidentified Ca^{2+} ion bound to ATP, in addition to the canonical Ca^{2+} ion bound within the Walker A motif and required for ATP hydrolysis.

The structure showed that the second metal ion contacts simultaneously ATP and the DNA-binding L2 loop in the adjacent RAD51 protomer (Figure 1E). Thus, its location allows it to fulfill concurrently three related functions: to sense the hydrolysis state of the filament by contacting the gamma phosphate, to modulate the affinity of RAD51 for DNA by affecting the conformation of the L2 loop and to strengthen the association between proximal RAD51 molecules in the filament. Together, these interactions provide the basis for a metal-dependent mechanism of coupling the hydrolysis state of the nucleotide to the filament's ability to bind DNA. By interacting with the carbonyl moieties of residues A293, H294, and S296, the metal ion helps nucleate the folding of the short alpha helix spanning residues G289 to A295 ($\alpha_{289\text{-}295}$) that anchors the L2 loop to the core of the RAD51 ATPase domain (Figure 1E). This alpha helix has a crucial role in linking DNA binding to the ATP

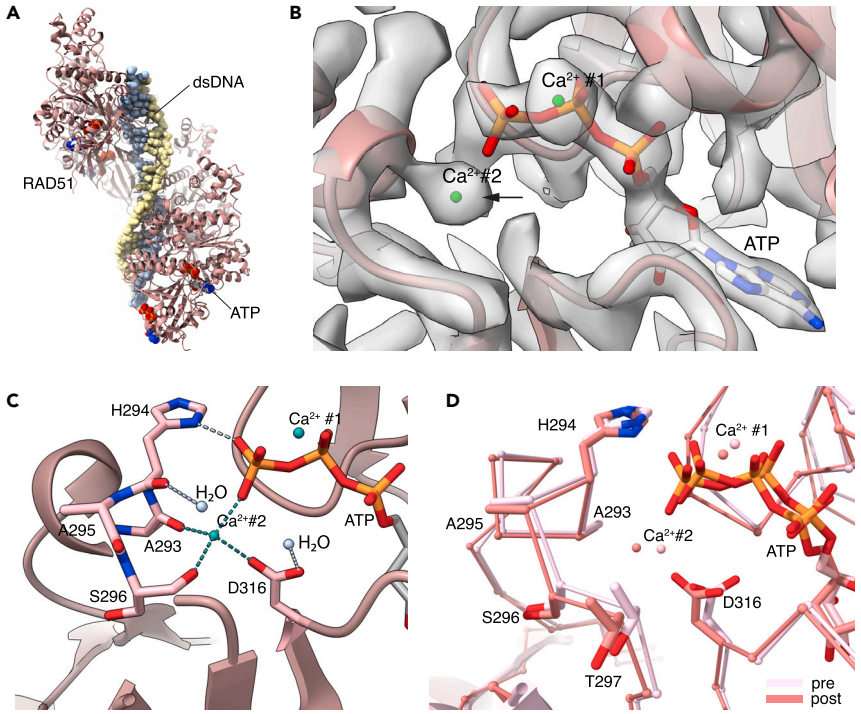


Figure 2. The second metal cation in the post-synaptic RAD51 filament

(A) CryoEM structure of the human RAD51-dsDNA-ATP filament. RAD51 is shown as ribbons, dsDNA and ATP as spacefill models.

(B) CryoEM map at the ATP site, with the density peak for the second Ca^{2+} ion marked by an arrow. The two Ca^{2+} cations are drawn as green spheres.

(C) Molecular details of the interactions of the second Ca^{2+} cation with ATP and the main-chain and side-chain atoms of surrounding RAD51 residues. The two Ca^{2+} cations are drawn as green spheres. The amino acids that interact with Ca^{2+} and ATP are shown in stick representation. The rest of the RAD51 is drawn as a light brown ribbon. The interactions of the second Ca^{2+} cation with the gamma phosphate of ATP, the carbonyl groups of A293, S296 and the carboxylate group of D316 are highlighted as green dashed lines. The hydrogen bond of the H294 side chain imidazole with the gamma phosphate and of two water molecules with the main-chain carbonyl group of H294 and the carboxylate of D316 are also shown.

(D) Superposition of pre- and post-synaptic filament structures, illustrating the high degree of similarity at the ATP-binding site. RAD51 is shown as an alpha carbon trace and relevant side chains are drawn explicitly in stick representation. The pre-synaptic structure is drawn in light pink and the post-synaptic structure in darker pink.

moiety: at its N-end, G289, N290, and I291 pack against the phosphate backbone of the DNA while at its C-end the imidazole ring in the side chain of H294 hydrogen bonds to the gamma phosphate.

These results show that the second metal ion promotes the active state of the RAD51 filament, by inducing the ATP-dependent conformation of the L2 loop that is required for DNA binding.

The second metal ion is present in the post-synaptic RAD51 filament

To determine whether the second metal ion is present in a RAD51 filament containing dsDNA, which is thought to represent the post-synaptic state of the filament after completion of strand-exchange, we examined the 2.9 Å cryoEM structure of human RAD51 bound to dsDNA and ATP in the same Ca^{2+} buffer (Figures 2A and S2, Table S1, STAR Methods). To capture a bona fide post-synaptic filament state, we incubated RAD51 with ssDNA and a dsDNA that contained a central mismatched region with perfect complementarity for the ssDNA (see STAR Methods). The resulting high-resolution structure showed clear, continuous density for dsDNA, as expected for a post-synaptic filament.

The structure of the post-synaptic NPF was highly similar to that of the pre-synaptic NPF, in agreement with what has been previously reported.[15] Inspection of the ATP-binding site revealed an unexplained density peak at the same position as in the pre-synaptic filament (Figure 2B), indicating the presence of a bound metal ion that was

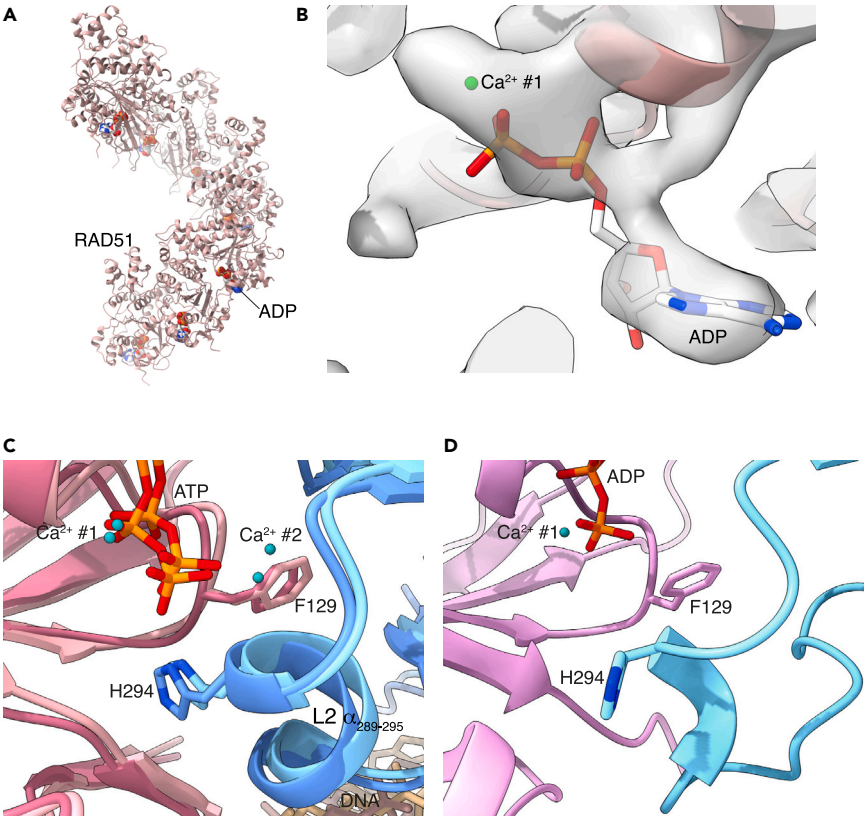


Figure 3. CryoEM structure of the RAD51-ADP filament

(A) Ribbon representation of the ADP-bound RAD51 filament.

(B) CryoEM map at the ADP site. The position of the Ca^{2+} cation bound within the Walker A motif is shown as a green sphere. Panels (C and D) show the side-chain conformations of F129 in the L2 loop in the presence of ATP and ADP, respectively. In the pre- and post-synaptic filaments (panel C), the F129 side chain packs against the alpha helix spanning residues 289–295, helping to stabilize the L2 conformation that is conducive to DNA binding. In the ADP-bound filament (panel D), the F129 side chain adopts a rotameric position made accessible by the lack of the gamma phosphate and second metal ion, and that contributes to altering the L2 conformation. Panels (C and D) are drawn in the same way, with the RAD51 protomers shown as pink and blue ribbons, the side chains of F129, H294, ATP, and ADP drawn explicitly in stick representation, and the Ca^{2+} cations as green spheres.

engaged in the same set of interactions as observed in the pre-synaptic filament structure. The higher resolution of the post-synaptic structure confirmed the gamma phosphate of ATP, the carbonyl groups of A293, S296, and the side-chain carboxylate of D316 of the adjacent RAD51 molecule as the coordinating oxygen atoms (Figure 2C). This apparent tetrahedral coordination is likely to be completed with water molecules to give more common bipyramidal coordination, which would also be the favored coordination of a physiological Mg^{2+} ion.

These findings show that the second metal ion is present and bound in the same fashion to both pre- and post-synaptic filaments (Figure 2D). It is therefore likely that the second metal ion is present throughout the reactions of homology search and strand exchange, to maintain the L2 loop in the required conformation for DNA binding.

Structure of the ADP-bound filament

As the metal ion is directly coordinated by the gamma phosphate of ATP, a prediction of our findings is that it will be lost once ATP is hydrolyzed to ADP. We prepared a RAD51 NPF sample in the presence of dsDNA and ADP in Ca^{2+} buffer, to mimic a post-synaptic filament that had hydrolyzed ATP and determined its cryoEM structure at 3.6 Å resolution (Figures 3A and S3, Table S1, STAR Methods). 3D classification showed that, relative to the pre- and post-synaptic NPFs, the ADP-bound filament displayed an increase in protomer rise and a decrease in twist angle. Inspection of the map at the ATP-binding site showed the presence

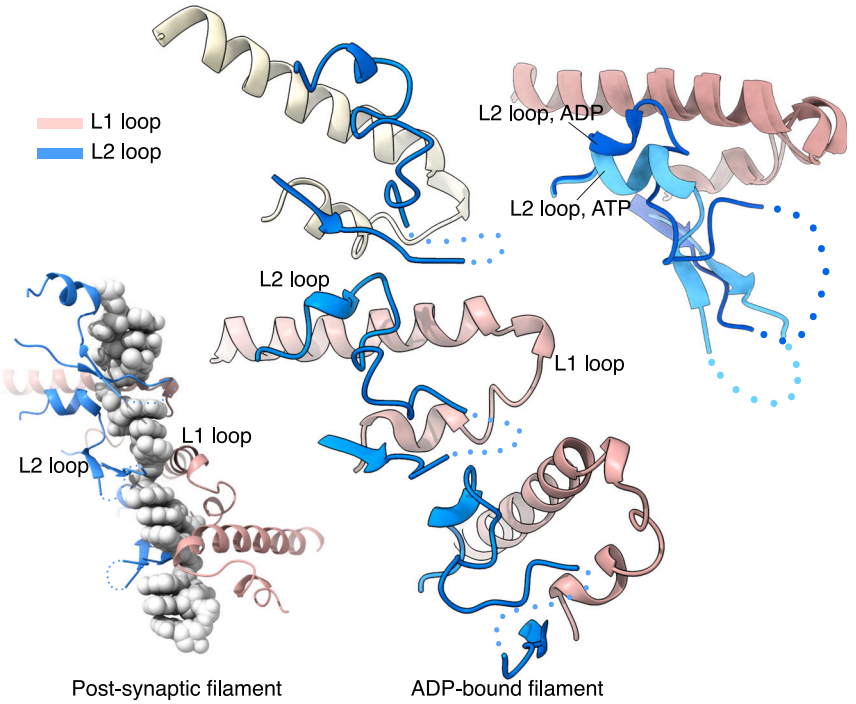


Figure 4. Comparison of the L1 and L2 loop conformations in the RAD51-ADP and post-synaptic filaments
In the central panel, the L1 and L2 loops for three adjacent protomers of the ADP-bound RAD51 filament are shown, drawn as light brown (L1) and light blue (L2) ribbons. For comparison, the arrangement of the L1 and L2 loops in the structure of the post-synaptic filament is shown in the bottom left panel, colored in the same way; only one strand of DNA is shown, as spacefill model. The top right panel shows a superposition of the L1 and L2 loops in the post-synaptic and ADP filaments, to highlight the different conformation of the L2 loop in the two structures. The L2 loop is in darker blue in the ADP-bound filament and in lighter blue in the post-synaptic filament, whereas the L1 loop is shown in light brown. In the three panels, the missing segment at the tip of the L2 loop is drawn as dots.

of the canonical metal ion in the Walker A motif but no density peak for the second metal ion (Figure 3B), as expected because of the missing gamma phosphate.

The structure further showed that the conformation of the L2 loop had drastically altered. The side chain of F129 in the Walker A motif, which packs against A293 of the adjacent protomer in the ATP-bound filament, had rotated to partially fill the gap left by the missing gamma phosphate (Figures 3C and 3D). The steric hindrance of the new F129 rotamer caused the helical residues at the C-end of the L2 loop to swing away and partially unfold. Surprisingly, rather than becoming disordered, the L2 loop transitioned to a compact random-coil conformation (Figure 4), anchored by hydrophobic interactions of I287, I291, I292, and P286 to the ATPase domain (Figure S4A). The new L2 trajectory appears to be incompatible with DNA binding due to steric clashes with the phosphoester backbone (Figure S4B), and in fact no density for DNA was observed in any of the 3D classes. We surmise that DNA must have dissociated from RAD51 during incubation prior to grid freezing as a result of the conformational change in L2. It is also possible that the DNA remains weakly associated with the filament in a range of conformations that are not detectable by cryoEM.

These findings show that the presence of the second metal ion depends on the hydrolysis state of the bound nucleotide and that ATP hydrolysis promotes a conformational change in the L2 loop, with ensuing loss of DNA binding. Thus, the structure of the ADP-bound filament identifies an intermediate state of the filament, where DNA has dissociated and the filament appears poised for disassembly.

DISCUSSION

The presence of a second metal ion in RAD51 filaments had not been reported before, even though cryoEM structures of pre- and post-synaptic RAD51 NPFs have been published.[15] It is likely that the resolution of

these structures was insufficient for the identification of the metal ion in the map. However, we found clear evidence for it in a recent cryoEM map of a pre-synaptic RAD51 filament at 2.97 Å (EMD 31158, PDB 7EJC),[30] and in reconstructions of pre- and post-synaptic filaments of RAD51's meiotic ortholog DMC1 (pre-synaptic: EMD 30311, PDB 7C9C at 3.33 Å; post-synaptic: EMD 31154, PDB 7EJ7 at 3.41 Å)[31] in agreement with our observation, although the authors did not discuss it (Figure S5).

The location and binding mode of an additional metal ion at the ATP site in human RAD51 NPFs resemble closely earlier reports of two potassium ions bound to the non-hydrolyzable ATP analog adenylylimidodiphosphate (AMP-PNP) in the crystallographic filament form of archeal RadA.[27] The interactions of one of the potassium ions with RadA and the nucleotide are very similar to the ones we observe for the second Ca^{2+} ion in the RAD51 filament. Indeed, the authors showed that two potassium ions observed in the crystallographic RadA filament can be replaced by one Ca^{2+} ion, with similar stimulatory effects on strand-exchange activity.[32] The promiscuity in the nature of the metal ion bound at the second site indicates that its function is to provide a positive charge that interacts favorably with the negatively charged C-end of L2's $\alpha_{289\text{-}295}$ helix rather than a direct involvement in ATP hydrolysis, which would require a specific geometry of coordinating ligands. This argument is supported by the observation that a D316K mutation in human RAD51 stabilizes the NPF and improves its recombinase function, and that the equivalent D302K mutation in archeal RadA forms active NPFs in the absence of salt.[33,34]

Thus, the presence of the second metal ion in the RAD51 NPF confirms and extends to eukaryotic RAD51 the mechanism first proposed for how DNA binding by archeal RadA is coupled to the hydrolysis state of the nucleotide: in the presence of ATP, the metal ion acts as a folding catalyst for the L2 loop, by helping specify its required conformation for DNA binding. This observation provides a structural rationale for the biochemical evidence that high concentrations of potassium and ammonium salts stimulate RAD51 activity[35,36]; it also agrees with molecular dynamics simulations showing that the presence of a second metal ion is necessary to keep the L2 loop in a conformation competent for ssDNA binding.[37] Conversely, loss of the gamma phosphate after ATP hydrolysis causes release of the second ion and impairment of DNA binding, as the L2 loop is no longer maintained in the correct conformation for interaction with DNA. Although in this study we have used Ca^{2+} to promote stability of the filament, we expect that the proposed mechanism will hold true for Mg^{2+}, which is more abundant in the cell and is supposed to be the physiological metal ion.

The cryoEM structure of the ADP-bound filament further shows that, rather than becoming disordered, the L2 loop takes up a new conformation that appears incompatible with DNA binding because of a steric clash with DNA. Thus, the identification of an ADP-bound filament intermediate that has dissociated from DNA provides a structural explanation for the requirement of ATP hydrolysis to license the disassembly of the post-synaptic RAD51 filament (Figure 5). The increased conformational freedom acquired by the L2 loop upon release from its ATP-dependent DNA-binding conformation is consistent with a passive mode of DNA dissociation, in agreement with single-molecule observations that filament dissociation after ATP hydrolysis tends to be slow and incomplete.[38,39] As ATP hydrolysis takes place randomly throughout the filament,[40] RAD51 dissociation from DNA is not cooperative; filament clearing from the DNA might be accelerated by accessory factors such as the human RAD54 translocase[23,41,42] or the worm helq-1 helicase.[43] Alternatively, or in addition to licensing NPF disassembly, ATP hydrolysis might signal the completion of the strand-exchange reaction: in this model, random events of ATP hydrolysis along the filament would alter the L2 conformation and thus prevent further recombination, by making the filament architecture incompatible with the mechanism of strand-exchange.

Taking past and present evidence together, the metal ion-dependent mechanism for coupling ATP hydrolysis state to DNA binding and filament disassembly is now well-defined. However, an important question remains concerning the nature of the molecular determinants that prevent ATP hydrolysis within the filament until completion of strand-exchange and that might promote ATP hydrolysis afterward. The cryoEM structures of pre- and post-synaptic filaments do not provide insight into this as they are essentially identical; indeed, dsDNA stimulates ATP hydrolysis by RAD51 to a lesser degree than ssDNA.[40,44] As all aspects of RAD51 activity are subject to strict control in the cell, it is possible that the specific intervention of accessory factors might be required to repress ATP hydrolysis in the pre-synaptic filament and to stimulate it in the post-synaptic filament. The RAD51 paralogues have been reported to promote RAD51 filament activity in several ways, including filament assembly, remodeling and stabilization of its active conformation[45–48]; however, no role in controlling the rate of ATP

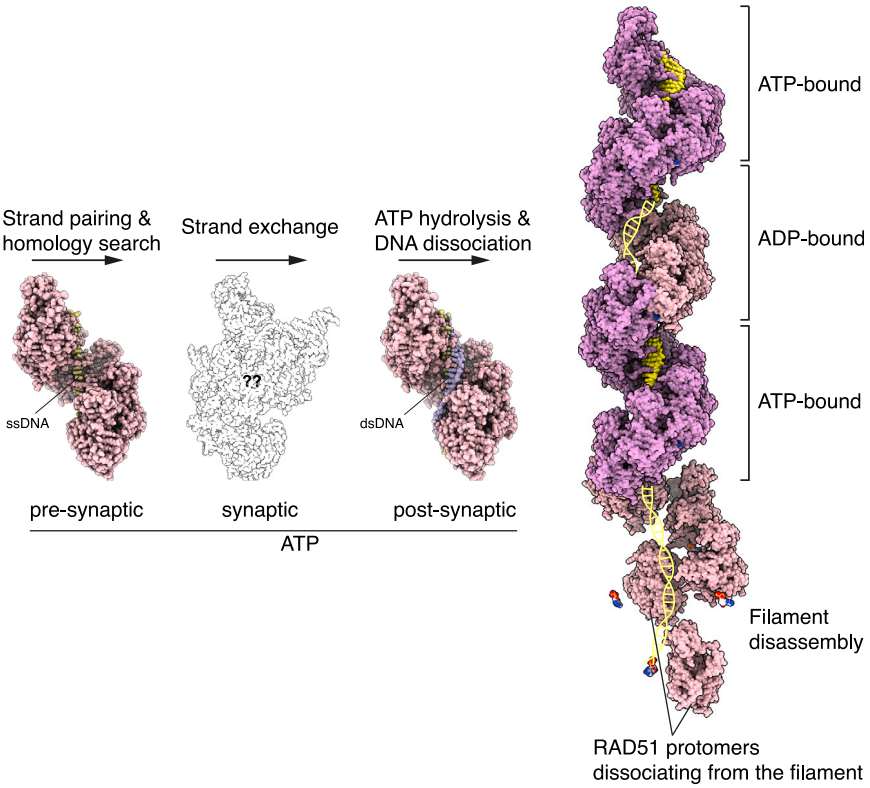


Figure 5. Structures of key RAD51 filament intermediates in the strand-exchange reaction

After completion of strand exchange, ATP hydrolysis at random points along the filament triggers dissociation of RAD51 from DNA, leading to segments of ATP-bound interspersed with DNA-free ADP-bound filament. ADP-bound RAD51 protomers that are licensed for disassembly dissociate from the filament end. RAD51 and DNA are shown as spacefill models, colored pink for RAD51, pale yellow for ssDNA and pale yellow and mauve for the dsDNA strands. The pre-, post- and ADP-bound filaments correspond to cryoEM structures described in this work. The structure of the RAD51 synaptic filament is not known; an outline of the structure of bacterial RecA bound to a D loop DNA is shown instead (PDB ID 7IY9).

hydrolysis of the filament has yet been ascribed to them, although Xrcc2 can stimulate the ATPase activity of RAD51,[49] and the Swi5-Sfr1 heterodimer promotes strand-exchange by RAD51 in an ATP hydrolysis-dependent mechanism.[50] Further work will be required to clarify the mechanisms that regulate ATP hydrolysis within the RAD51 NPF.

Limitations of the study

Our study does not formally identify the atomic species responsible for the density peak which we assign to a Ca^{2+} cation. Furthermore, we assume that the likely physiologically relevant cation Mg^{2+} will be bound to the filament in the same way as Ca^{2+}.

STAR★METHODS

Detailed methods are provided in the online version of this paper and include the following:

- KEY RESOURCES TABLE
- RESOURCE AVAILABILITY
  - Lead contact
  - Materials availability
  - Data and code availability
- EXPERIMENTAL MODEL DETAILS
- METHOD DETAILS
  - Expression and purification of human Rad51 protein
  - Vitrification of RAD51 filament grids

- CryoEM data collection and processing
- Model building and refinement
- Electrophoretic mobility shift assay (EMSA)

SUPPLEMENTAL INFORMATION

Supplemental information can be found online at https://doi.org/10.1016/j.isci.2023.106689.

ACKNOWLEDGMENTS

We would like to thank Joseph Maman for helpful comments on the manuscript, and Steve Hardwick for help with cryoEM data collection. Funding for the experiments reported in the paper was provided by MRC grants MR/N000161/1, MR/S021248/1 and Wellcome Trust grant 221892/Z/20/Z to L.P., and by a BBSRC DTP studentship to R.A.

AUTHOR CONTRIBUTIONS

R.A. determined the structures of the post- and ADP filaments, assisted by L.J.. D.B. determined the structure of the pre-synaptic filament. L.P. directed the project and wrote the manuscript, with input from all authors.

DECLARATION OF INTERESTS

The authors declare no competing interests.

INCLUSION AND DIVERSITY

We support inclusive, diverse, and equitable conduct of research.

Received: December 2, 2022
Revised: March 21, 2023
Accepted: April 13, 2023
Published: April 25, 2023

REFERENCES

1. San Filippo, J., Sung, P., and Klein, H. (2008). Mechanism of eukaryotic homologous recombination. Annu. Rev. Biochem. *77*, 229–257. https://doi.org/10.1146/annurev.biochem.77.061306.125255.

2. Prakash, R., Zhang, Y., Feng, W., and Jasin, M. (2015). Homologous recombination and human health: the roles of BRCA1, BRCA2, and associated proteins. Csh Perspect Biol *7*, a016600. https://doi.org/10.1101/cshperspect.a016600.

3. Wright, W.D., Shah, S.S., and Heyer, W.-D. (2018). Homologous recombination and the repair of DNA double-strand breaks. J. Biol. Chem. *293*, 10524–10535. https://doi.org/10.1074/jbc.tm118.000372.

4. Jasin, M., and Rothstein, R. (2013). Repair of strand breaks by homologous recombination. Csh Perspect Biol *5*, a012740. https://doi.org/10.1101/cshperspect.a012740.

5. Ait Saada, A., Lambert, S.A.E., and Carr, A.M. (2018). Preserving replication fork integrity and competence via the homologous recombination pathway. DNA Repair *71*, 135–147. https://doi.org/10.1016/j.dnarep.2018.08.017.

6. Tye, S., Ronson, G.E., and Morris, J.R. (2021). A fork in the road: where homologous recombination and stalled replication fork protection part ways. Semin. Cell Dev. Biol. *113*, 14–26. https://doi.org/10.1016/j.semcdb.2020.07.004.

7. Zickler, D., and Kleckner, N. (2015). Recombination, pairing, and synapsis of homologs during meiosis. Cold Spring Harbor Perspect. Biol. *7*, a016626. https://doi.org/10.1101/cshperspect.a016626.

8. Sansam, C.L., and Pezza, R.J. (2015). Connecting by breaking and repairing: mechanisms of DNA strand exchange in meiotic recombination. FEBS J. *282*, 2444–2457. https://doi.org/10.1111/febs.13317.

9. Story, R.M., Weber, I.T., and Steitz, T.A. (1992). The structure of the E. coli recA protein monomer and polymer. Nature *355*, 318–325.

10. Di Capua, E., Engel, A., Stasiak, A., and Koller, T. (1982). Characterization of complexes between recA protein and duplex DNA by electron microscopy. J. Mol. Biol. *157*, 87–103. https://doi.org/10.1016/0022-2836(82)90514-9.

11. Ogawa, T., Yu, X., Shinohara, A., and Egelman, E.H. (1993). Similarity of the yeast RAD51 filament to the bacterial RecA filament. Science *259*, 1896–1899. https://doi.org/10.1126/science.8456314.

12. Yu, X., Jacobs, S.A., West, S.C., Ogawa, T., and Egelman, E.H. (2001). Domain structure and dynamics in the helical filaments formed by RecA and Rad51 on DNA. Proc. Natl. Acad. Sci. USA *98*, 8419–8424. https://doi.org/10.1073/pnas.111005398.

13. Conway, A.B., Lynch, T.W., Zhang, Y., Fortin, G.S., Fung, C.W., Symington, L.S., and Rice, P.A. (2004). Crystal structure of a Rad51 filament. Nat. Struct. Mol. Biol. *11*, 791–796. https://doi.org/10.1038/nsmb795.

14. Chen, Z., Yang, H., and Pavletich, N.P. (2008). Mechanism of homologous recombination from the RecA–ssDNA/dsDNA structures. Nature *453*, 484–489. https://doi.org/10.1038/nature06971.

15. Xu, J., Zhao, L., Xu, Y., Zhao, W., Sung, P., and Wang, H.-W. (2017). Cryo-EM structures of human RAD51 recombinase filaments during catalysis of DNA-strand exchange. Nat. Struct. Mol. Biol. *24*, 40–46. https://doi.org/10.1038/nsmb.3336.

16. Sung, P., and Stratton, S.A. (1996). Yeast Rad51 recombinase mediates polar DNA strand exchange in the absence of ATP hydrolysis*. J. Biol. Chem. *271*, 27983–27986. https://doi.org/10.1074/jbc.271.45.27983.

17. Chi, P., Van Komen, S., Sehorn, M.G., Sigurdsson, S., and Sung, P. (2006). Roles of

ATP binding and ATP hydrolysis in human Rad51 recombinase function. DNA Repair *5*, 381–391. https://doi.org/10.1016/j.dnarep.2005.11.005.

18. Bugreev, D.V., and Mazin, A.V. (2004). Ca2+ activates human homologous recombination protein Rad51 by modulating its ATPase activity. Proc. Natl. Acad. Sci. USA *101*, 9988–9993. https://doi.org/10.1073/pnas.0402105101.

19. Morgan, E.A., Shah, N., and Symington, L.S. (2002). The requirement for ATP hydrolysis by Saccharomyces cerevisiae Rad51 is bypassed by mating-type heterozygosity or RAD54 in high copy. Mol. Cell Biol. *22*, 6336–6343. https://doi.org/10.1128/mcb.22.18.6336-6343.2002.

20. Stark, J.M., Pierce, A.J., Oh, J., Pastink, A., and Jasin, M. (2004). Genetic steps of mammalian homologous repair with distinct mutagenic consequences. Mol. Cell Biol. *24*, 9305–9316. https://doi.org/10.1128/mcb.24.21.9305-9316.2004.

21. Morrison, C., Shinohara, A., Sonoda, E., Yamaguchi-Iwai, Y., Takata, M., Weichselbaum, R.R., and Takeda, S. (1999). The essential functions of human Rad51 are independent of ATP hydrolysis. Mol. Cell Biol. *19*, 6891–6897. https://doi.org/10.1128/mcb.19.10.6891.

22. Namsaraev, E.A., and Berg, P. (1998). Binding of Rad51p to DNA interaction of Rad51p with single- and DOUBLE-STRANDED DNA. J. Biol. Chem. *273*, 6177–6182. https://doi.org/10.1074/jbc.273.11.6177.

23. Li, X., Zhang, X.-P., Solinger, J.A., Kiianitsa, K., Yu, X., Egelman, E.H., and Heyer, W.-D. (2007). Rad51 and Rad54 ATPase activities are both required to modulate Rad51-dsDNA filament dynamics. Nucleic Acids Res. *35*, 4124–4140. https://doi.org/10.1093/nar/gkm412.

24. Ristic, D., Modesti, M., van der Heijden, T., van Noort, J., Dekker, C., Kanaar, R., and Wyman, C. (2005). Human Rad51 filaments on double- and single-stranded DNA: correlating regular and irregular forms with recombination function. Nucleic Acids Res. *33*, 3292–3302. https://doi.org/10.1093/nar/gki640.

25. van Mameren, J., Modesti, M., Kanaar, R., Wyman, C., Peterman, E.J.G., and Wuite, G.J.L. (2009). Counting RAD51 proteins disassembling from nucleoprotein filaments under tension. Nature *457*, 745–748. https://doi.org/10.1038/nature07581.

26. Wu, Y., He, Y., Moya, I.A., Qian, X., and Luo, Y. (2004). Crystal structure of archaeal recombinase RadA A snapshot of its extended conformation. Mol. Cell *15*, 423–435. https://doi.org/10.1016/j.molcel.2004.07.014.

27. Wu, Y., Qian, X., He, Y., Moya, I. a, and Luo, Y. (2005). Crystal structure of an ATPase-active form of Rad51 homolog from Methanococcus voltae. Insights into potassium dependence. J. Biol. Chem. *280*, 722–728. https://doi.org/10.1074/jbc.m411093200.

28. Shim, K.-S., Schmutte, C., Yoder, K., and Fishel, R. (2006). Defining the salt effect on human RAD51 activities. DNA Repair *5*, 718–730. https://doi.org/10.1016/j.dnarep.2006.03.006.

29. Sigurdsson, S., Trujillo, K., Song, B., Stratton, S., and Sung, P. (2001). Basis for avid homologous DNA strand exchange by human Rad51 and RPA. J. Biol. Chem. *276*, 8798–8806.

30. Xu, J., Zhao, L., Peng, S., Chu, H., Liang, R., Tian, M., Connell, P.P., Li, G., Chen, C., and Wang, H.-W. (2021). Mechanisms of distinctive mismatch tolerance between Rad51 and Dmc1 in homologous recombination. Nucleic Acids Res. *49*, 13135–13149. https://doi.org/10.1093/nar/gkab1141.

31. Luo, S.-C., Yeh, H.-Y., Lan, W.-H., Wu, Y.-M., Yang, C.-H., Chang, H.-Y., Su, G.-C., Lee, C.-Y., Wu, W.-J., Li, H.-W., et al. (2021). Identification of fidelity-governing factors in human recombinases DMC1 and RAD51 from cryo-EM structures. Nat. Commun. *12*, 115. https://doi.org/10.1038/s41467-020-20258-1.

32. Qian, X., He, Y., Ma, X., Fodje, M.N., Grochulski, P., and Luo, Y. (2006). Calcium stiffens archaeal Rad51 recombinase from methanococcus voltae for homologous recombination. J. Biol. Chem. *281*, 39380–39387. https://doi.org/10.1074/jbc.m607785200.

33. Amunugama, R., He, Y., Willcox, S., Forties, R.A., Shim, K.-S., Bundschuh, R., Luo, Y., Griffith, J., and Fishel, R. (2012). RAD51 protein ATP cap regulates nucleoprotein filament stability. J. Biol. Chem. *287*, 8724–8736. https://doi.org/10.1074/jbc.m111.239426.

34. Qian, X., He, Y., Wu, Y., and Luo, Y. (2006). Asp302 determines potassium dependence of a RadA recombinase from methanococcus voltae. J. Mol. Biol. *360*, 537–547. https://doi.org/10.1016/j.jmb.2006.05.058.

35. Sigurdsson, S., Trujillo, K., Song, B., Stratton, S., and Sung, P. (2001). Basis for avid homologous DNA strand exchange by human Rad51 and RPA. J. Biol. Chem. *276*, 8798–8806. https://doi.org/10.1074/jbc.m010011200.

36. Liu, Y., Stasiak, A.Z., Masson, J.-Y., McIlwraith, M.J., Stasiak, A., and West, S.C. (2004). Conformational changes modulate the activity of human RAD51 protein. J. Mol. Biol. *337*, 817–827. https://doi.org/10.1016/j.jmb.2004.02.022.

37. Fornander, L.H., Frykholm, K., Reymer, A., Renodon-Cornière, A., Takahashi, M., and Nordén, B. (2012). Ca 2+ improves organization of single-stranded DNA bases in human Rad51 filament, explaining stimulatory effect on gene recombination. Nucleic Acids Res. *40*, 4904–4913. https://doi.org/10.1093/nar/gks140.

38. Hilario, J., Amitani, I., Baskin, R.J., and Kowalczykowski, S.C. (2009). Direct imaging of human Rad51 nucleoprotein dynamics on individual DNA molecules. Proc. Natl. Acad. Sci. USA *106*, 361–368. https://doi.org/10.1073/pnas.0811965106.

39. Miné, J., Disseau, L., Takahashi, M., Cappello, G., Dutreix, M., and Viovy, J.-L. (2007). Real-time measurements of the nucleation, growth and dissociation of single Rad51–DNA nucleoprotein filaments. Nucleic Acids Res. *35*, 7171–7187. https://doi.org/10.1093/nar/gkm752.

40. Tombline, G., and Fishel, R. (2002). Biochemical characterization of the human RAD51 protein I. ATP hydrolysis*. J. Biol. Chem. *277*, 14417–14425. https://doi.org/10.1074/jbc.m109915200.

41. Solinger, J.A., Kiianitsa, K., and Heyer, W.-D. (2002). Rad54, a swi2/snf2-like recombinational repair protein, Disassembles rad51:dsDNA filaments. Mol. Cell *10*, 1175–1188. https://doi.org/10.1016/s1097-2765(02)00743-8.

42. Mason, J.M., Dusad, K., Wright, W.D., Grubb, J., Budke, B., Heyer, W.-D., Connell, P.P., Weichselbaum, R.R., and Bishop, D.K. (2015). RAD54 family translocases counter genotoxic effects of RAD51 in human tumor cells. Nucleic Acids Res. *43*, 3180–3196. https://doi.org/10.1093/nar/gkv175.

43. Ward, J.D., Muzzini, D.M., Petalcorin, M.I.R., Martinez-Perez, E., Martin, J.S., Plevani, P., Cassata, G., Marini, F., and Boulton, S.J. (2010). Overlapping mechanisms promote postsynaptic RAD-51 filament disassembly during meiotic double-strand break repair. Mol. Cell *37*, 259–272. https://doi.org/10.1016/j.molcel.2009.12.026.

44. Sung, P. (1994). Catalysis of ATP-dependent homologous DNA pairing and strand exchange by yeast RAD51 protein. Science *265*, 1241–1243. https://doi.org/10.1126/science.8066464.

45. Taylor, M.R.G., Špírek, M., Jian Ma, C., Carzaniga, R., Takaki, T., Collinson, L.M., Greene, E.C., Krejci, L., and Boulton, S.J. (2016). A polar and nucleotide-dependent mechanism of action for RAD51 paralogs in RAD51 filament remodeling. Mol. Cell *64*, 926–939. https://doi.org/10.1016/j.molcel.2016.10.020.

46. Taylor, M.R.G., Špírek, M., Chaurasiya, K.R., Ward, J.D., Carzaniga, R., Yu, X., Egelman, E.H., Collinson, L.M., Rueda, D., Krejci, L., and Boulton, S.J. (2015). Rad51 paralogs remodel pre-synaptic Rad51 filaments to stimulate homologous recombination. Cell *162*, 271–286. https://doi.org/10.1016/j.cell.2015.06.015.

47. Roy, U., Kwon, Y., Marie, L., Symington, L., Sung, P., Lisby, M., and Greene, E.C. (2021). The Rad51 paralog complex Rad55-Rad57 acts as a molecular chaperone during homologous recombination. Mol. Cell *81*, 1043–1057.e8. https://doi.org/10.1016/j.molcel.2020.12.019.

48. Belan, O., Barroso, C., Kaczmarczyk, A., Anand, R., Federico, S., O'Reilly, N., Newton, M.D., Maeots, E., Enchev, R.I., Martinez-Perez, E., et al. (2021). Single-molecule analysis reveals cooperative stimulation of Rad51 filament nucleation and growth by

mediator proteins. Mol. Cell *81*, 1058–1073.e7. https://doi.org/10.1016/j.molcel.2020.12.020.

49. Shim, K.S., Schmutte, C., Tombline, G., Heinen, C.D., and Fishel, R. (2004). hXRCC2 enhances ADP/ATP processing and strand exchange by hRAD51. J. Biol. Chem. *279*, 30385–30394. https://doi.org/10.1074/jbc.m306066200.

50. Ito, K., Murayama, Y., Takahashi, M., and Iwasaki, H. (2018). Two three-strand intermediates are processed during Rad51-driven DNA strand exchange. Nat. Struct. Mol. Biol. *25*, 29–36. https://doi.org/10.1038/s41594-017-0002-8.

51. Zadeh, J.N., Steenberg, C.D., Bois, J.S., Wolfe, B.R., Pierce, M.B., Khan, A.R., Dirks, R.M., and Pierce, N.A. (2011). NUPACK: analysis and design of nucleic acid systems. J. Comput. Chem. *32*, 170–173. https://doi.org/10.1002/jcc.21596.

52. Zivanov, J., Nakane, T., Forsberg, B.O., Kimanius, D., Hagen, W.J., Lindahl, E., and Scheres, S.H. (2018). New tools for automated high-resolution cryo-EM structure determination in RELION-3. Elife *7*, e42166. https://doi.org/10.7554/elife.42166.

53. Zheng, S.Q., Palovcak, E., Armache, J.-P., Verba, K.A., Cheng, Y., and Agard, D.A. (2017). MotionCor2: anisotropic correction of beam-induced motion for improved cryo-electron microscopy. Nat. Methods *14*, 331–332. https://doi.org/10.1038/nmeth.4193.

54. Rohou, A., and Grigorieff, N. (2015). CTFFIND4: fast and accurate defocus estimation from electron micrographs. J. Struct. Biol. *192*, 216–221. https://doi.org/10.1016/j.jsb.2015.08.008.

55. Adams, P.D., Afonine, P.V., Bunkóczi, G., Chen, V.B., Davis, I.W., Echols, N., Headd, J.J., Hung, L.W., Kapral, G.J., Grosse-Kunstleve, R.W., et al. (2010). PHENIX: a comprehensive Python-based system for macromolecular structure solution. Acta Crystallogr. D Biol. Crystallogr. *66*, 213–221. https://doi.org/10.1107/s0907444909052925.

56. Brouwer, I., Moschetti, T., Candelli, A., Garcin, E.B., Modesti, M., Pellegrini, L., Wuite, G.J., and Peterman, E.J. (2018). Two distinct conformational states define the interaction of human RAD51-ATP with single-stranded DNA. Embo J *37*, e98162. https://doi.org/10.15252/embj.201798162.

57. Emsley, P., and Cowtan, K. (2004). Coot: model-building tools for molecular graphics. Acta Crystallogr. D Biol. Crystallogr. *60*, 2126–2132.

STAR★METHODS

KEY RESOURCES TABLE

REAGENT or RESOURCE	SOURCE	IDENTIFIER
Bacterial and virus strains		
Rosetta2(DE3) E.coli	Millipore Sigma	#71-402-3
Chemicals, peptides, and recombinant proteins		
RAD51 protein	This study	
Deposited data		
RAD51 pre-synaptic filament structure	This study	PDB: 8BQ2
RAD51 pre-synaptic filament map	This study	EMDB: 16170
RAD51 post-synaptic filament structure	This study	PDB: 8BR2
RAD51 post-synaptic filament map	This study	EMDB: 16197
RAD51 ADP-bound filament structure	This study	PDB: 8BSC
RAD51 ADP-bound filament map	This study	EMDB: 16224
Oligonucleotides		
x60	IDT	ATGGTGTGTGTAGGTTAATGT GAGGAGGAGAGGTGAAGAA GGAGGAGAGAAGAAGGAGGC
cx60	IDT	GCCTCCTTCTTCTCTCCTCCTTC TTCACCTCTCCTCCTCACATT AACCTACACACACCAT
R51-16-SL	IDT	GGCGTAGCCCAATCGTGTGG TACTGGGCCCGTAGGG
R51-14	IDT	TGGAGGTGCATCGAGCTCG CGACAAACCTTCTATGT TGAGCGTCAGTCGG
R51-15	IDT	CCGACTGACGCTCAACAT AGGTACCACACGGCGAGC TCGATGCACCTCCA
Recombinant DNA		
pMBP4-R51	Brouwer et al., 2018[56]	
Software and algorithms		
Relion3.1	Zivanov et al., 2018[52]	
Phenix	Adams et al., 2010[55]	
Coot	Emsley and Cowtan 2004[57]	
MotionCor2	Zheng et al., 2017[53]	
CTFFIND4	Rohou and Grigorieff, 2015[54]	

RESOURCE AVAILABILITY

Lead contact

Further information and requests for resources and reagents should be directed towards, and will be fulfilled by, the lead contact, Luca Pellegrini (lp212@cam.ac.uk).

Materials availability

This study did not generate any new unique reagents.

Data and code availability

- Structure coordinates and post-processed cryoEM maps have been deposited in the PDB and EMDB databases and are publicly available as of the date of publication. Accession numbers are listed in the key resources table.
- This paper does not report original code.
- Any additional information required to re-analyze the data reported in this paper is available from the lead contact upon request.

EXPERIMENTAL MODEL DETAILS

Rosetta2 E.coli were used to express recombinant protein. Cells were cultured in 2YT media at 37 degrees shaking at 175 rpm.

METHOD DETAILS

Expression and purification of human Rad51 protein

Calcium chloride-washed competent *Rosetta2 E.coli* cells were transformed with plasmid pMBP4-RAD51, for co-expression of human RAD51 and His_6-MBP-BRCA2 BRC4. Transformants were selected by culturing on agar plates containing 50 mg/ml kanamycin. Transformants were resuspended in 2YT culture media and used to inoculate 1L cultures of 2YT culture media containing 50 mg/ml kanamycin. Cells were cultured at 37°C until an OD_{600} of 0.7 was reached, before induction with 0.5 mM IPTG. Cultures were then incubated overnight at 15°C before harvesting. Cell pellets were resuspended in resuspension buffer (500 mM NaCl, 50 mM HEPES pH 7.4) before flash freezing in liquid nitrogen for storage or used immediately for protein purification.

Cell pellets were defrosted and 1 tablet of sigma EDTA-free protease inhibitor cocktail was added per 50 ml of resuspended cells. Cells were lysed by sonication on ice and lysate was centrifuged (40,000*g*, 1 hr, 4°C) to remove cell debris. Lysate supernatant was loaded on a HisTrap HP 5 ml column preequilibrated with His Buffer A (20 mM HEPES pH 7.5, 300 mM NaCl, 5 % glycerol) before isocratic elution in 40 % His Buffer B (20 mM HEPES pH 7.5, 300 mM NaCl, 5 % glycerol, 500 mM imidazole). Eluted fractions were pooled and diluted in 1 ml batches by dropwise addition of a total of 3 ml of A125 Buffer (20 mM HEPES pH 7.5, 125 mM NaCl, 5 % glycerol, 2 mM DTT) while mixing. Diluted protein was loaded on a HiTrap Heparin 5 ml column preequilibrated with A125 buffer using a peristaltic pump at 4°C, before a gradient elution of 12.5 % to 100 % buffer A1000 (20 mM HEPES pH 7.5, 1 M NaCl, 5 % glycerol, 2 mM DTT). Fractions containing RAD51 were concentrated to 2 ml using an Amicon 10,000 MWCO concentrator before purification by size exclusion using a Superdex200pg gel filtration column preequilibrated with RAD51 storage buffer (20 mM HEPES pH 7.5, 300 mM NaCl, 5 % Glycerol, 2 mM DTT). Eluted fractions containing RAD51 were pooled, concentrated to a final concentration of 85 μM, snap frozen in liquid nitrogen and stored at -80°C.

Vitrification of RAD51 filament grids

Pre-synaptic filament

10 μM RAD51 was incubated briefly on ice with a DNA 60mer (x60) in a buffer containing 20 mM TrisCl pH 7.5, 100 mM NaCl, 0.5 mM ATP, 5 mM $CaCl_2$ prior to vitrification. The nucleotide sequence of the DNA was designed to avoid secondary structure propensity, using NUPACK.[51] Cryo-EM grids were prepared by pipetting 3 μl of sample on a R1.2/1.3 Cu 300 mesh grid (Quantifoil) and plunge-freezing in liquid ethane using a Vitrobot Mark IV (ThermoFisher).

Post-synaptic and ADP-bound filaments

5 μM RAD51 protein was incubated with DNA in a buffer containing 150 mM NaCl, 25 mM HEPES pH 7.5, 5 mM $CaCl_2$, 2 mM DTT. The sample was supplemented with either 2 mM ATP or 2 mM ADP for the formation of post-synaptic- or ADP-containing filaments.

For the preparation of post-synaptic filaments, the sample containing RAD51 was first incubated with 250 nM ssDNA-16SL for 15 minutes at 25 °C followed by incubation with 250 nM annealed R51-14:R51-15 dsDNA for

15 minutes at 25 °C before vitrification. Glutaraldehyde was added 3 minutes prior to grid freezing to a final concentration of 0.05 %.

For the preparation of RAD51 ADP-bound filaments, annealed x60:cx60 dsDNA was added to the RAD51 reaction mix and incubated for 15 minutes at 25 °C prior to vitrification.

UltrAuFoil R1.2/R1.3 300 mesh gold grids (Quantifoil) were glow-discharged twice (once on each side) for 1 minute using a PELCO easiGlow system (0.4 mBar, 25 mA, negative polarity). 6 μl of reaction mix was applied to each grid before plunge-freezing in liquid ethane using a Vitrobot Mark IV robot (ThermoFisher), set to 100 % humidity, 4 °C, 2 second blot time and -8 blot force.

All DNA oligonucleotides were purchased PAGE-purified from IDT and resuspended to 100mM in TE buffer. DNA was annealed in TE buffer to a final concentration of 10 μM dsDNA by boiling at 95 °C for 5 minutes followed by slow cooling to room temperature. All DNA sequences can be found in the key resources table.

CryoEM data collection and processing

Information about the data processing for the pre-, post- and ADP-bound filaments can be found in Table S1 and Figures S1–S3.

Pre-synaptic filament

Data were collected on a Titan Krios microscope fitted with a Falcon III detector using the EPU package (FEI), at the Microscopy facility of the Nanoscience Center. Data was processed using Relion 3.0.[52] Micrograph motion correction was performed using MotionCor2[53] and CTF estimation was performed using CTFFIND4.[54] 850,217 particles were extracted using auto-picked coordinates and 723,142 particles were retained after rounds of 2D classification to remove badly aligned averages. An initial 3D model was generated from a subset of 5000 particles and subject to 3D classification. This initial 3D class was used for further 3D classification of the entire dataset, yielding three classes with very similar helical parameters. 3D class 2 with the best rotational accuracy was used as reference for 3D auto-refinement of the entire dataset, which converged at 4.2 Å. A second round of 3D auto-refinement after movie refinement and particle polishing improved the resolution to 4.1 Å. The map was further improved by masking and post-processing to a final resolution of 3.8 Å.

Post-synaptic and ADP-bound filaments

RAD51 grids were screened using a Talos Arctica microscope fitted with a Falcon III detector, and data were collected on a Titan Krios microscope fitted with a Gatan K3 detector at the Cryo-EM facility in the Department of Biochemistry. Data was processed using Relion 3.1.[52] Micrograph motion correction was performed using MotionCor2[53] and CTF estimation was performed using CTFFIND4.[54] Autopicking was performed based on manually picked 2D class averages with a picking threshold of 0.1. Autopicked particles were extracted with a box size of 260Å for the RAD51 post-synaptic filament and 200Å for the ADP-bound RAD51 filament and binned 4x and 2x respectively. 2D classification was performed iteratively on extracted particles with the option to ignore CTF correction until the first peak selected in addition to processing using 'fast subsets'.

For the RAD51 post-synaptic filament, 543,102 high-resolution particles were identified following three rounds of single-particle 2D classification and were used to generate an initial 3D model. Single-particle 3D classification produced highly anisotropic, poorly aligned classes, so particles were re-extracted and binned 4x and used to refine the initial 3D model, which was globally sharpened using Relion 3.1 to a final resolution of 2.9 Å.

For the RAD51 ADP-bound filament, 62,657 high-resolution particles were identified following 3 rounds of 2D classification and were used to generate a 3D initial model. A first round of 3D classification using helical reconstruction (5 classes) generated three helical 3D models, all of which were unbound with DNA and exhibited helical parameters in the range 52.9-56.0 for twist and 18.3-19.4 Å for rise. 3D classification was repeated using one of the previous 3D classes as a starting model which generated four high-resolution helical classes. These four 3D classes were extracted and binned 2x, yielding 40,481 particles which were

used for refinement of the highest-resolution 3D class (class 2) to 4.9 Å, followed by global sharpening and density modification with *phenix.resolve_cryoem*[55] to produce a map at 3.6 Å resolution.

Model building and refinement

In all cases, RAD51-ATP protomers were individually fitted in the final filament maps, using the crystallographic coordinates of the human RAD51-ATP structure in filament form (PDB ID 5NWL).[56] For the pre-synaptic NPF, a ssDNA 30mer consisting of a tandem repeat of three GGA nucleotides was generated in Coot[57] and fitted in the map. GGA was chosen as the consensus RAD51-binding site, based on the nucleotide frequency in the 20 RAD51-binding sites present in the ssDNA 60mer. For the post-synaptic NPF, a double-stranded DNA sequence corresponding to a fully complementary portion of the R51-14:R51-15 duplex was fitted in the map.

Fitting of the filament models to the map was improved using real-space refinement as implemented in Phenix.[55] For all filament models, the two protomers occupying the outermost positions in the map were left out of the final refined model as they had poorer model-to-map correlation coefficients.

Electrophoretic mobility shift assay (EMSA)

EMSA reactions were prepared in buffer: 25mM HEPES pH 7.5, 150 mM NaCl, 2 mM DTT, 5 mM $CaCl_2$, supplemented with either 2 mM ATP or a titration of 0.5, 1, 2, 5, 10 mM ADP. Fluorescein-labeled dx60 : cdx60 dsDNA was added to a final concentration of 500 nM and incubated with RAD51 at a final concentration of 10 μM at 25 °C for 15 minutes prior to loading. Immediately before loading, samples were mixed with a 0.5:1 volume of 50 % (w/v) sucrose solution. Samples were run on a pre-run 0.5 % agarose gel in 0.5x TB buffer (45 mM Tris, 45 mM boric acid) for 2.5hr at 4°C and 35V. The gel was imaged using a Typhoon FLA9000 by excitation at 473 nm.